Open Ceramics 5 (2021) 100060

Contents lists available at ScienceDirect

Open Ceramics

journal homepage: www.editorialmanager.com/oceram

Unraveling the hardening mechanism during laser-induced slip casting of lithium aluminate-microsilica slurry

Sebastian Simon *, Gregor J.G. Gluth

Bundesanstalt für Materialforschung und -prüfung (BAM), Unter den Eichen 87, 12205, Berlin, Germany

ARTICLE INFO

Keywords:
Alkali-activated materials
Additive manufacturing
Laser-induced slip casting
Lithium
Layered double hydroxide

ABSTRACT

Additive manufacturing (AM) of alkali-activated materials is a promising method for producing ceramic precursors, construction elements and other parts. A recently introduced AM process is laser-induced slip casting of lithium aluminate/microsilica slurries, which yields parts with excellent mechanical strengths. To clarify the underlying mechanisms, μ-Raman spectroscopy was applied to parts produced by the process, and the dissolution and hydration of lithium aluminate was studied inter alia using conventional and in-situ X-ray diffraction. The results show that significant dissolution of lithium aluminate occurs, particularly at increased temperatures during laser interaction, which leads to an increase of pH and precipitation of an akopovaite-like Li-Al-CO_3 layered double hydroxide. The increase of the pH is likely to induce dissolution of the microsilica and possibly formation of a hydrous lithium aluminosilicate gel. These observations explain the strength evolution of the studied parts and can also aid the development and improvement of related AM methods.

1. Introduction

Additive manufacturing (AM) of ceramic material systems gained a lot of interest over the last years and has been employed using different AM technologies with various starting materials. Examples of indirect technologies are powder based selective laser sintering (SLS) of Al_2O_3 [1] and SiC [2]; slurry based SLS of Al_2O_3/SiO_2 mixtures [3] and lithium aluminosilicate glasses and glass ceramics [4]; laminated object manufacturing (LOM) of SiC [5] and glass ceramics [6]; and stereolithography of Ca-phosphate based materials [7]. Direct inkjet printing (DIP) of oxides and non-oxides suspension [8] and direct ink writing ('Robocasting') of alumina-gels [9] belong to the direct technologies.

In parallel, AM of building materials in general [10] and in particular AM of alkali-activated materials (AAMs) like direct 3D printing of NaOH activated fly ash [11] and alkali-borosilicate solution activated blast furnace slag [12] has received considerable attention in the last years. Furthermore, direct ink writing of NaOH and sodium silicate-activated metakaolin [13,14] are objects of ongoing research in the building materials community. AAMs have been recognized as a promising construction material for 3D printing process due to their fast-setting, cost-effective and ecofriendly nature [15]. Apart from these characteristics, the fire resistance [16,17] and durability [18–20] of geopolymers can make them superior to the conventional cement composites in specific applications.

AAMs are typically amorphous aluminosilicate materials formed when a solid precursor (coal fly ash, blast furnace slag, metakaolin) dissolves in alkaline solutions (alkali hydroxide, alkali silicate, alkali carbonate etc.) and, through condensation reactions and polymerization, gives rise to a network responsible for the setting of the system. The main reaction product is determined to a large extent by the amount of calcium in the system, with Ca-rich systems (e.g., based on blast furnace slag) generally leading to poorly crystalline calcium aluminosilicate hydrates (C-A-S-H) as the major reaction products, and Ca-poor systems (e.g., based on metakaolin) leading to amorphous or semi-crystalline alkali aluminosilicate hydrates (N-A-S-H). These latter materials, commonly known as "geopolymers", form a three-dimensional tetrahedral network of $(Al,Si)O_4$ in which charge balance is achieved by the presence of the alkali metal cations such as Na or K [21]. The formation of viable Li-AAMs by this method is more difficult, probably because of the lower pH-value of the lithium silicate solutions, resulting in the much slower dissolution of solid silica in lithium silicate or LiOH than is the case with Na- or K-dominated solutions. O'Connor and MacKenzie [22] reported a method to form a lithium aluminosilicate inorganic polymer (LAS IP) *via* an alternative synthesis route involving solid-state reaction between halloysite and LiOH to give a hydraulically active product that sets upon the addition of a small amount of water. Subsequently, Nourbakhsh et al.

* Corresponding author.
E-mail address: sebastian.simon@bam.de (S. Simon).

https://doi.org/10.1016/j.oceram.2021.100060
Received 1 December 2020; Received in revised form 14 January 2021; Accepted 14 January 2021
Available online 21 January 2021

[23] used this solid state method to produce amorphous LAS IP as a precursors for the silicothermal reaction of crystalline LAS and LAS matrix composites with Al_2O_3. The silicon was added after the solid-state generation of the LAS IP but prior to its hydration and firing, since otherwise the additional elementary silicon would oxidize under the strongly alkaline conditions of conventional geopolymer synthesis. Karrech et al. [24] employed lithium aluminosilicate residue (LASR) as precursor for a LAS IP. They found that LASR had a low reactivity, but a mix of 50% LASR and 50% granulated blast furnace slag exhibited increased reactivity, and a three times higher strength than for conventional concrete could be obtained. O'Connor and MacKenzie [22] mentioned that none of their cured samples showed the amorphous character of a true geopolymer, and most of them contained crystalline lithium zeolites. However, as an analog to conventional geopolymers, an amorphous lithium aluminosilicate hydrate (L-A-S-H) gel should form as reaction product.

Hlaváček et al. [25] presented a novel method for additive manufacturing of Li-activated AAMs with laser-induced slip casting (LIS). In this method, a lithium aluminate/microsilica slurry is deposited layer-wise and selectively heated by laser radiation to induce hardening reactions of the material; subsequently, the produced element is further cured at slightly elevated temperature for 24 h. The process yielded materials with comparatively high mechanical strengths (max. compressive strength 49 MPa, and max. flexural strength 11.6 MPa), but it remained unclear which phases are responsible for the strength development of the obtained AAMs. The previous XRD investigations indicated that the crystalline phase assemblage of the products did not differ considerably from the starting materials, and a possible L-A-S-H gel formation could not be unequivocally proven.

Here, we present μ-Raman spectroscopy results for LIS-produced materials of Hlaváček et al. [25] in order to identify which phase formed as binder between microsilica and lithium aluminate. According to the literature, γ-$LiAlO_2$ is almost insoluble in water at room temperature [26]. To assess which phases can form during the printing process, we determined how much lithium and aluminum is released into solution as a function of temperature. Additionally, possible amorphous and crystalline reaction products were synthesized in order to collect Raman reference spectra to aid in identifying the composition of the binder phase.

2. Material and methods

2.1. The LIS process

The starting materials for the slurries were lithium aluminate (Sigma-Aldrich, St. Louis, MO, USA), microsilica (SiO_2 'RW-Füller', RW silicium GmbH, Pocking, Germany), and quartz flour as filler (Quarzmehl W 3, Quarzwerke GmbH, Frechen/plant Weferlingen, Germany). The lithium aluminate consisted mainly of γ-$LiAlO_2$ (PDF # 00-038-1464); in addition it contained small amounts of the spinel $LiAl_5O_8$ (PDF # 00-038-1425) as well as minor quantities of $Li_2Al_4(OH)_{12}(CO_3)\cdot 3H_2O$ (PDF # 00-037-0728), corundum (α-Al_2O_3; PDF # 00-046-1212) and bayerite (α-$Al(OH)_3$; PDF # 00-020-0011) (Table 2). The microsilica was virtually fully amorphous, including only very minor amounts of silicon carbide (PDF # 00-049-1429), and silicon (PDF # 00-001-0787) or quartz (PDF # 00-046-1045) impurities. It consisted of spherical primary particles with diameters of about 50–300 nm, which formed larger agglomerates. The quartz flour was virtually pure quartz (PDF # 00-046-1045); its nominal particle size range was 0–250 μm (manufacturer's data).

Slurries were produced by first blending dry lithium aluminate and microsilica in amounts to yield an overall SiO_2/Al_2O_3 molar ratio of 3.5. The slurries were produced by blending lithium aluminate/microsilica mixes with an equal mass of quartz flour and subsequent mixing of the resulting powder with deionized water at a water/solids ratio (w/s) of 0.50 with a conventional laboratory mixer for cement mortars ('RILEM mixer'). Immediately after mixing, the slurries were subjected to LIS for manufacturing of parts. The LIS process is an iteration of the deposition of a layer of slurry and subsequent local heating of the desired geometry in this layer by a laser beam. The detailed printing process was described by Hlaváček et al. [25]. Examples of manifolds produced by the LIS process from lithium aluminate/microsilica slurries are shown in Fig. 1.

2.2. Synthesis of the reference materials

Li–Al–CO_3 layered double hydroxide, $Li_2Al_4(OH)_{12}(CO_3)\cdot 3H_2O$, was prepared by the sol-gel method described by Cheng et al. [27]. 12 g Lithium hydroxide monohydrate, ($LiOH\cdot H_2O$; Honeywell Fluka, Muskegon, MI, USA) were dissolved in 100 ml distilled water, and 30 g of bayerite (α-$Al(OH)_3$; Bernd Kraft, Duisburg, Germany) were added to the LiOH solution to obtain a mixture, which was stirred at 80 °C to get a well-dispersed sol. To yield the product, the water in the sol was evaporated at 80 °C overnight. As carbonate for the formation of the compound is provided by atmospheric CO_2, which dissolves in the aqueous solution, no solid carbonate was required in the starting materials.

L-A-S-H gel with a nominal Li:Al:Si elemental ratios of 1:1:1.85 was synthesized using the organic steric entrapment route described by Walkley et al. [28]. A 5 wt% polyethylene glycol (PEG) solution was produced by adding small increments of PEG (Sigma Aldrich, St. Louis, MO, USA) to ultrapure water and the resultant solution was stirred at 60 °C for 1 h. Aluminium nitrate nonahydrate ($Al(NO_3)_3\cdot 9H_2O$; Honeywell Fluka, Muskegon, MI, USA) and lithium nitrate trihydrate ($LiNO_3\cdot 3H_2O$; Merck, Billerica, MA, USA) were each added to distilled water to produce 40 wt% solutions by mass of anhydrous salt, and these solutions were subsequently added to the 5 wt% PEG solution and stirred at 60 °C for 1 h. Subsequently, colloidal silica (40 wt% SiO_2 in water; Ludox HS-40 colloidal; Sigma Aldrich, St. Louis, MO, USA) was added to the mixture. Water was evaporated from the resulting solution by stirring at 80 °C to form a viscous gel which was then placed in an oven at 100 °C overnight to remove any remaining water and nitrates.

2.3. Determination of lithium aluminate solubility

According to the literature, γ-$LiAlO_2$ is almost insoluble in water at room temperature [26]. Hlaváček et al. [25] mentioned that the temperature during the printing process could reach 100 °C at the surface. To identify which phase can form during the printing process, it is necessary to clarify how much Li and Al is released into solution as a function of temperature. For this purpose, 5 g lithium aluminate were added to 100 g ultrapure water and stirred at room temperature, 50 °C or 80 °C. After 2 h, the suspension was filtered, and the pH value of the filtrate was determined with a calibrated pH probe. Additionally, the concentration of Li and Al in the filtrate was determined by ICP-OES (Thermo Fisher Scientific iCAP 6000; Waltham, MA, USA). As reference, the Li and Al concentration of the ultrapure water was determined. The filter residue was dried in vacuum (~40 mbar) for 2 days and its composition determined with XRD (Section 2.5).

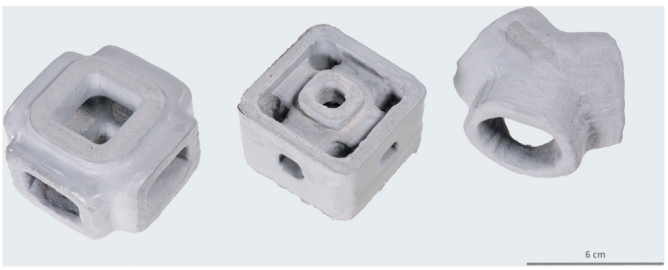

Fig. 1. Examples of manifolds produced from lithium aluminate/microsilica slurries with the LIS-process described by Hlaváček et al. [25].

2.4. Raman spectroscopy

Raman spectra were obtained using a confocal Alpha300R instrument (WITec, Germany) with an excitation wavelength of 532 nm and a power of 4 mW at room temperature. The spectrometer grating had 600 lines/mm, giving a ~4.5 cm^{-1} spectral resolution. A 100-× objective resulting in a diameter of the incident focused laser beam of ~1 µm was employed. Raman maps were acquired by moving the sample stage in 0.5-µm increments in the x- and y-direction along the surface of the samples to acquire the area of interest with an accumulation time of 0.2 s per spectra. Additional spectra were acquired with 50 s accumulation time each. Measurements were performed in the region from 200 cm^{-1}–4000 cm^{-1}.

Background correction and normalization was carried out with the Witec software Project Four80/160. The false-colored Raman mapping was carried out with a window of 2 cm^{-1} by attributing a color to the main spectral peak of each phase: microsilica (blue, 1331 cm^{-1}), lithium aluminate (green, 508 cm^{-1}), quartz (yellow, 462 cm^{-1}), binder phase (red, 1087 cm^{-1}).

2.5. X-ray diffraction

To collect XRD patterns, a conventional laboratory X-ray diffractometer with Bragg-Brentano geometry (Rigaku Ultima IV, Tokyo, Japan) with Cu Kα and D-Tex silicon strip detector was used. The measurement was carried out with a front-loading sample holder. To illuminate only the center of the sample holder, a divergence slit of 0.5° and a horizontal divergence slit of 10 mm were used. A beam knife was installed to prevent low-angle scattering. All diffractograms were recorded from 5° to 65° 2θ, with a step width of 0.02° and a scan speed of 0.5° 2 θ/min. To increase the diffraction statistics, a spinning sample holder with a speed of 15 revolutions per minute (rpm) was employed. To evaluate the diffraction data, the Match! Software [29] in combination with the powder diffraction file PDF-2 (2003) database [30] was used.

To clarify whether carbonation, oxidation, or both, during the sample preparation has an influence on the phase development, in-situ XRD investigations were carried out at room temperature. Lithium aluminate pastes with w/s = 0.50 were produced and placed in a Teflon container which was either covered with a Kapton film or measured without covering. One measurement every 7 min was recorded in the range 8°–38° 2θ, with a step width of 0.1° and a scan speed of 3.3° 2θ/min.

2.6. TGA/DTG measurements

For thermogravimetric analysis (TGA), a STA 449C System from Netzsch was used. The sample material was heated from 35 °C to 1000 °C, with a heating rate of 10 °C/min and a nitrogen flow of 80 ml/min. For each measurement 35 mg of the sample material was filled in an Al_2O_3 crucible and placed in the TGA system. To eliminate oxygen and to prevent any oxidation process during the measurement, the furnace was first evacuated and subsequently filled with nitrogen. From the recorded TGA curves, their derivatives (DTG curves) were computed and plotted.

3. Results and discussion

3.1. Synthesis of $Li_2Al_4(OH)_{12}(CO_3)\cdot 3H_2O$ and L-A-S-H gel

The XRD evaluation of the final product of the synthesis of the Li–Al–CO_3 layered double hydroxide is shown in Fig. 2. The product consists mainly of $Li_2Al_4(OH)_{12}(CO_3)\cdot 3H_2O$ (PDF # 00-037-0728), lower amounts of LiOH (PDF # 01-085-1064) and γ-$LiAlO_2$ (PDF # 00-033-0785), and traces of gibbsite (γ-$Al(OH)_3$; PDF # 01-070-2038) and Li_2CO_3 (PDF # 00-022-1141). LiOH and $Al(OH)_3$ are either remaining starting materials or have recrystallized, while γ-$LiAlO_2$ is newly formed during the synthesis, as Cheng et al. [27] already reported for their investigation. In the following, the synthetic Li–Al–CO_3 layered double hydroxide will be referred to as $Li_2Al_4(OH)_{12}(CO_3)\cdot 3H_2O$, as this was the major phase in the product.

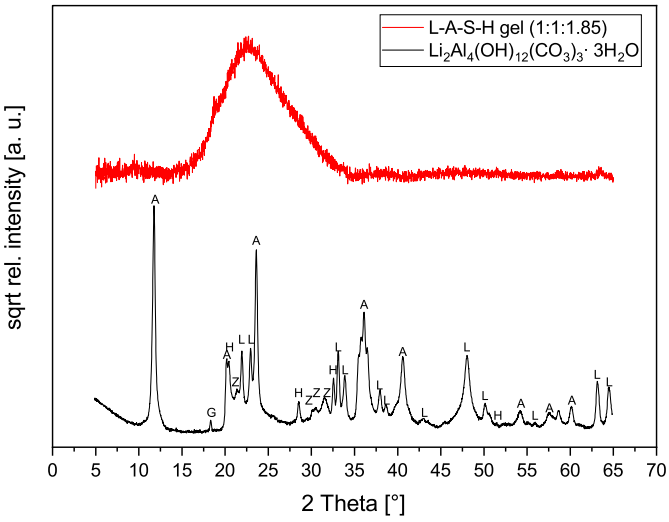

Fig. 2. Diffractograms of the synthesized Li–Al–CO_3 layered double hydroxide and the L-A-S-H gel with phase assignment. The Li–Al–CO_3 layered double hydroxide consists of $Li_2Al_4(CO_3)(OH)_{12}\cdot 3H_2O$ (A), LiOH (H), γ-$LiAlO_2$ (L) and minor amounts of gibbsite γ-$Al(OH)_3$ (G) and $LiCO_3$ (Z). Intensities are plotted on a square-root scale to emphasize smaller peaks, that would be difficult to discern if the intensities were reported on a linear scale.

The XRD pattern of the L-A-S-H gel consists of an asymmetric broad diffraction peak between 15° and 35° 2θ with now sharp diffraction peaks, which confirms the amorphous character of the synthesized gel.

3.2. Raman spectroscopic investigation of the LIS-produced parts

To determine the relevant vibrational signatures for constructing the Raman maps, individual Raman spectra of the raw materials quartz, microsilica, lithium aluminate, synthetic $Li_2Al_4(OH)_{12}(CO_3)\cdot 3H_2O$ and synthetic L-A-S-H gel 1:1:1.85 were recorded (Fig. 3). In addition, spectra from the literature for the naturally occurring Li–Al–CO_3 layered double hydroxide akopovaite ($Li_2Al_4(OH)_{12}(CO_3)\cdot 3H_2O$) [31] and for zabuyelite ($LiCO_3$; RUFF-R100211) were obtained. The spectra for each phase show characteristic peaks in the high-frequency region and partially overlapping peaks in the low-frequency region. The peak positions of the

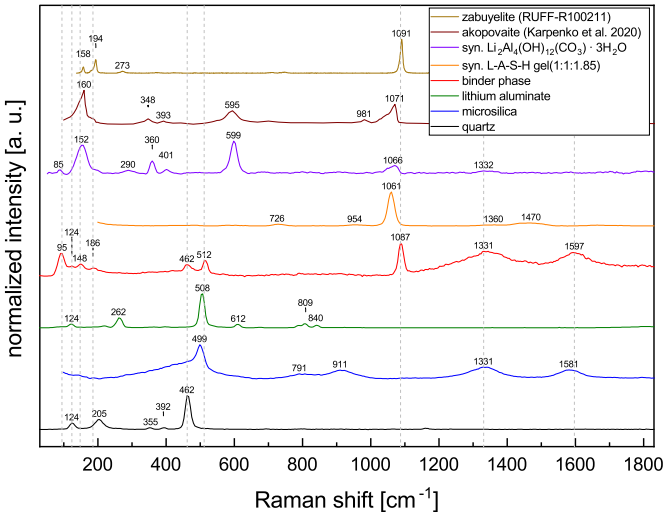

Fig. 3. Raman spectra of the binder phase, the raw materials for the LIS process (lithium aluminate, microsilica, quartz) and the reference materials (zabuyelite [Li_2CO_3], akopovaite, synthetic $Li_2Al_4(OH)_{12}(CO_3)\cdot 3H_2O$, L-A-S-H gel).

synthesized $Li_2Al_4(OH)_{12}(CO_3)\cdot 3H_2O$ are in good agreement with the peak positions of akopovaite reported by Karpenko et al. [31]. However, the relatively intensities are different.

The Raman maps were obtained by attributing a color to the characteristic spectral peak of each relevant phase: microsilica (blue, 1331 cm^{-1}), lithium aluminate (green, 508 cm^{-1}), quartz (yellow, 462 cm^{-1}) and the so called "binder phase" (red, 1087 cm^{-1}) according to the spectra in Fig. 3. The resulting maps which were collected at the surface of a polished LIS-produced AAM are shown in Fig. 4. The left picture displays a region next to a quartz grain as a representative overview of the sample. The right picture in Fig. 4 is a zoom-in detail of the red-colored area of the overview map. The increase of magnification reveals that the red areas are not homogeneous but that there are also small areas of microsilica and lithium aluminate. The red area between microsilica and lithium aluminate will further be addressed as the binder phase.

The spectra of this binder phase consist of unique spectral features that can be assigned to specific phases. The features at 1331 cm^{-1} and 1597 cm^{-1} can be assigned to microsilica, the features at 124 cm^{-1} and 512 cm^{-1} correspond to lithium aluminate, and the feature at 462 cm^{-1} is attributed to quartz. The features at 95 cm^{-1} and 148 cm^{-1} can be assigned to $Li_2Al_4(OH)_{12}(CO_3)\cdot 3H_2O$ (85 cm^{-1} and 152 cm^{-1} for the reference compound) and the feature at 186 cm^{-1} corresponds to Li_2CO_3 (194 cm^{-1} for the reference compound). The peak of the binder phase at 1087 cm^{-1} has no exact equivalent among the spectra of the reference materials, but it likely corresponds to the overlapping features of Li_2CO_3 (1091 cm^{-1}) and $Li_2Al_4(OH)_{12}(CO_3)\cdot 3H_2O$ (1066 cm^{-1}) or L-A-S-H gel (1061 cm^{-1}). Unfortunately, the low frequency region of the Raman spectrum of the L-A-S-H gel is not available due to strong fluorescence in this area, and the assignment with just one peak is ambiguous. Li_2CO_3 in the binder phase could have formed during the LIS process and subsequent hardening, or during sample preparation at the surface of the specimen for Raman spectroscopy. It is noted that, although the L-A-S-H gel synthesized in the present study exhibited its major Raman peak at 1061 cm^{-1}, amorphous lithium silicates in general may exhibit slightly different patterns: [32] and [33] reported for Q^3 Si species in their lithium silicate glasses a strong peak at 1084 cm^{-1} and 1090 cm^{-1}, respectively, which is closer to the Raman shift of the binder phase than the value for the L-A-S-H gel.

3.3. Determination of the solubility of lithium aluminate

The pH-value, Li- and Al-concentration for water and the filtrate at temperatures of 20 °C, 50 °C and 90 °C as well as the mass difference between the filter residue and the starting lithium aluminate is shown in Table 1. The pH-value of the filtrate increases with temperature from 12.0 at 20 °C to 12.3 at 50 °C and 12.5 at 80 °C. The concentrations of Li and Al in the filtrate at 20 °C are 38.4 mg/l and 67.6 mg/l, respectively. The concentrations of both elements increase with increasing temperature: At 50 °C, the concentration is almost twice as high, 75.3 mg/l for Li and 78.3 mg/l for Al, and at 80 °C the concentrations are 142.8 mg/l for Li and 150.5 mg/l for Al. This variation of the concentrations is reflected in the increase of the mass difference between the filter residue and the initial weight of the lithium aluminate with temperature: Whereas the difference is close to 0% at 20 °C, the mass loss increases to 1.1% at 50 °C and 3.8% at 80 °C. These results demonstrate that, in contrast to what is stated in pertinent handbooks [26], the solubility of γ-$LiAlO_2$ in water cannot be neglected already at room temperature, but even more so at higher temperatures.

Table 1
pH-value, Li and Al concentration of water and of the filtrate, and the mass difference between the filter residues and the starting lithium aluminate.

Temperature [°C]	pH-value	Li [mg/l]	Al [mg/l]	Δm Filter residue [%]
ultrapure water	6.9	<0.01	<0.01	–
20	12.0	38.4	67.6	0.2
50	12.3	75.3	78.3	−1.1
80	12.5	142.8	150.5	−3.8

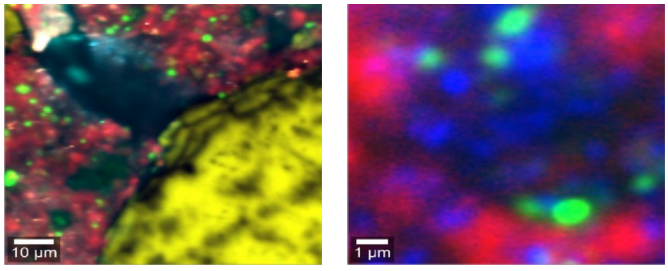

Fig. 4. Raman maps of a representative region next to a quartz grain (left) and a zoom into the binder phase (right). Raman maps were obtained by attributing a color to the main spectral peak of each phase: microsilica (blue, 1331 cm^{-1}), γ-$LiAlO_2$ (green, 508 cm^{-1}), quartz (yellow, 462 cm^{-1}), binder phase (red, 1087 cm^{-1}). (For interpretation of the references to color in this figure legend, the reader is referred to the Web version of this article.)

3.4. XRD and TGA/DTG examination of the filter residues

The XRD patterns of the lithium aluminate and the filter residues obtained at 20 °C, 50 °C and 80 °C are shown in Fig. 5. To examine the reactions that take place when lithium aluminate is suspended in water, the XRD patterns of the filter residues where evaluated using the reference intensity ratio (RIR) [34]; the results are listed in Table 2: α-$Al(OH)_3$ and Al_2O_3 do not dissolve to a significant extent, whereas the fraction of γ-$LiAlO_2$ in the filter residues decreases and the fraction of $Li_2Al_4(OH)_{12}(CO_3)\cdot 3H_2O$ increases with increasing temperature. In contrast, the fraction of $LiAl_2O_5$ in the filter residues increases with increasing temperature. This can be attributed to the fact that γ-$LiAlO_2$ dissolves in water but only part of the released Li and Al precipitates as $Li_2Al_4(OH)_{12}(CO_3)\cdot 3H_2O$, leading to a net loss of solid material (Table 2). Since the phase contents determined with the RIR method are normalized to 100%, the apparent content of $LiAl_2O_5$ in the filter residue thus increases, while there is in fact no formation of this phase during the dissolution experiments.

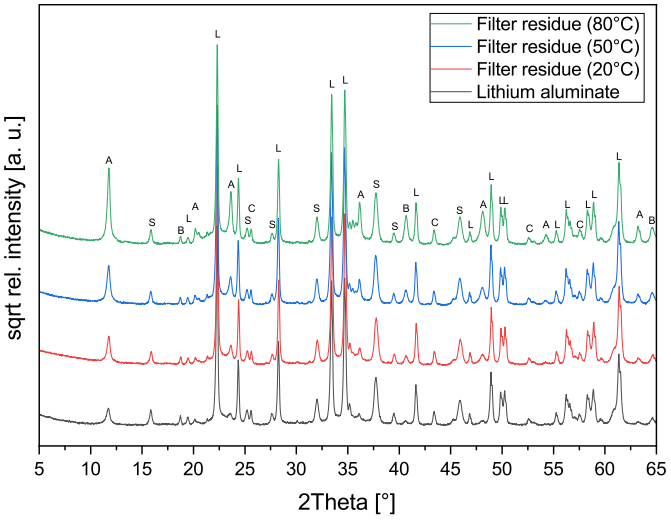

Fig. 5. Diffractograms of the filter residues obtained at different temperatures in comparison to the starting lithium aluminate. With increasing temperature, more γ-$LiAlO_2$ (L) dissolves, bayerite α-$Al(OH)_3$ (B) and corundum Al_2O_3 (C) remain almost unchanged, and the amount of $Li_2Al_4(OH)_{12}(CO_3)\cdot 3H_2O$ (A) and Li–Al spinel $LiAl_5O_8$ (S) in the filter residue increases with temperature. Intensities are plotted on a square-root scale to emphasize smaller peaks, that would be difficult to discern if the intensities were reported on a linear scale.

Table 2
Quantities (in wt%) of the phases present in the lithium aluminate and the filter residues as a function of temperature, determined using the RIR method.

Phase	γ-$LiAlO_2$	$Li_2Al_4(OH)_{12}(CO_3)\cdot 3H_2O$	$LiAl_5O_8$	Al_2O_3	α-$Al(OH)_3$
PDF #	00-038-1464	00-037-0728	00-038-1425	00-046-1212	01-077-0117
Lithium aluminate	93.0	1.2	4.8	0.9	0.1
Filter residue (20 °C)	92.0	2.9	4.7	0.3	0.1
Filter residue (50 °C)	78.9	8.4	11.8	0.9	0.1
Filter residue (80 °C)	70.3	18.1	10.6	0.8	0.1

In principle, it is difficult to distinguish between $LiAl_2(OH)_7\cdot 2H_2O$ (PDF # 00-040-0710) and $Li_2Al_4(CO_3)$ $(OH)_{12}\cdot 3H_2O$ (PDF # 00-037-0728) by means of their main XRD peaks, because there is significant overlap at 11.71, 20.13, 23.56, 40.66 and 48.05 °2θ (Cu Kα radiation). However, there are two minor peaks at 21.36 and 36.12 °2θ, that correspond to $Li_2Al_4(OH)_{12}(CO_3)\cdot 3H_2O$, thus allowing its identification. In the previous study [25], reported that the lithium aluminate contains $LiAl_2(OH)_7\cdot 2H_2O$, with this assignment based on only the major XRD peaks, while minor reflections where not considered. If instead $Li_2Al_4(OH)_{12}(CO_3)\cdot 3H_2O$ is used for the evaluation of the diffractograms, as in the present study, there is a perfect match and no peaks are missing. This finding proves that $Li_2Al_4(OH)_{12}(CO_3)\cdot 3H_2O$ is already present in the starting material, most likely formed by reaction of γ-$LiAlO_2$ with CO_2 and water from the air.

The TGA and DTG curves of the filter residues obtained at 20 °C, 50 °C and 80 °C are shown in Fig. 6. Three main stages of thermal decomposition can be discerned, with the second stage consisting of two partially overlapping steps. The total mass loss (at 1000 °C) increases systematically with increase of the temperature of the solubility experiment. In Table 3, the numerical evaluation of the combined TGA/DTG results is displayed. The temperatures for the three main thermal combustion stages result from the fitted maxima of the DTG curve, while the mass loss was determined from the TGA curve at the corresponding temperature. The decomposition steps could be assigned to $Li_2Al_4(OH)_{12}(CO_3))\cdot 3H_2O$ by comparison with values from the literature [35]. The small deviations between the peak temperatures in the present study and those of Drewien et al. [35] as well as the split of the second stage likely result from different experimental conditions and the presence of bayerite, which decomposes around 280 °C [36]. The total mass loss on heating to 1000 °C increased proportional to the contents of $Li_2Al_4(OH)_{12}(CO_3)\cdot 3H_2O$ determined by XRD for the different temperatures of the dissolution experiments, which is a further confirmation of this phase being formed in higher amounts at higher temperatures.

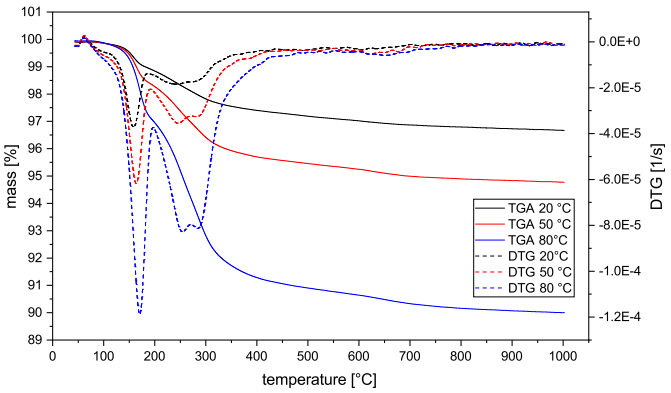

Fig. 6. Thermogravimetric analysis of the filter residues obtained at different temperatures. The curves show essentially three stages of weight loss, the total mass loss increasing with increasing temperature at which the solution test was performed.

3.5. *In-situ XRD investigation of lithium aluminate hydration*

Fig. 7 shows the results of the in-situ XRD investigation of the hydration of lithium aluminate pastes. Two experiments were performed, one in which the paste was covered with Kapton foil to prevent oxidation and carbonatation of the surface, and one without Kapton foil, i.e. with the paste exposed to the air. In both experiments, the γ-$LiAlO_2$ content decreases and $Li_2Al_4(OH)_{12}(CO_3)\cdot 3H_2O$ is formed. However, the experiment without Kapton foil reveal that $LiCO_3$ and an additional, unidentified phase have formed. This shows that $LiCO_3$ will only form in direct contact with air, while $Li_2Al_4(OH)_{12}(CO_3)\cdot 3H_2O$ is also formed when access of air is limited. As only $Li_2Al_4(OH)_{12}(CO_3)\cdot 3H_2O$ but no $LiCO_3$ was found in the Raman measurements (Section 3.2), it can be concluded that the $Li_2Al_4(OH)_{12}(CO_3)\cdot 3H_2O$ in the LIS-produced parts had formed during the LIS process and not only through contact of the specimen surfaces with air during sample preparation and handling.

4. Conclusions

Using μ-Raman spectroscopy, a distinct phase or phase mixture could be identified in the present study as the 'binder phase' between the lithium aluminate and microsilica particles in elements produced by laser-induced slip casting (LIS) of lithium aluminate/microsilica slurries. Based on comparison with spectra of reference compounds, the binder phase was determined to consist of $Li_2Al_4(OH)_{12}(CO_3)\cdot 3H_2O$, a akopovaite-like layered double hydroxide, and possibly a hydrous lithium aluminosilicate (L-A-S-H) gel.

Dissolution experiments show that γ-$LiAlO_2$ is more soluble than usually assumed and that its solubility increases with temperature, whereby the pH-value of the solution increases significantly. The Li and Al released during dissolution precipitates mainly as $Li_2Al_4(OH)_{12}(CO_3)\cdot 3H_2O$. In-situ XRD investigations of hydrating lithium aluminate pastes show that $LiCO_3$ forms only in direct contact with air. As only minor amounts of this compound where found in the binder phase, it can be concluded that the $Li_2Al_4(OH)_{12}(CO_3)\cdot 3H_2O$ in the LIS-produced materials is not an artefact of sample preparation. Since layered double

Table 3
Evaluation of the combined TGA/DTG investigations of the filter residues. The temperature of the maximum decomposition rate was determined by fitting the maxima of the DTG curves, the total mass loss for the corresponding temperature was determined from the TGA curves.

Filtration temperature	Temperature [°C] peakfit DTG	Ref. temperature [°C] (Drewien et al., 1996)	Species	Mass loss [%]
20 °C	158	177	H_2O	0.9
	243, 271	275	H_2O, CO_2	1.1
50 °C	163	177	H_2O	1.3
	245, 281	275	H_2O, CO_2	2.2
	648	632	CO_2	0.1
80 °C	170	177	H_2O	2.4
	254, 283	275	H_2O, CO_2	4.3
	650	632	CO_2	0.4

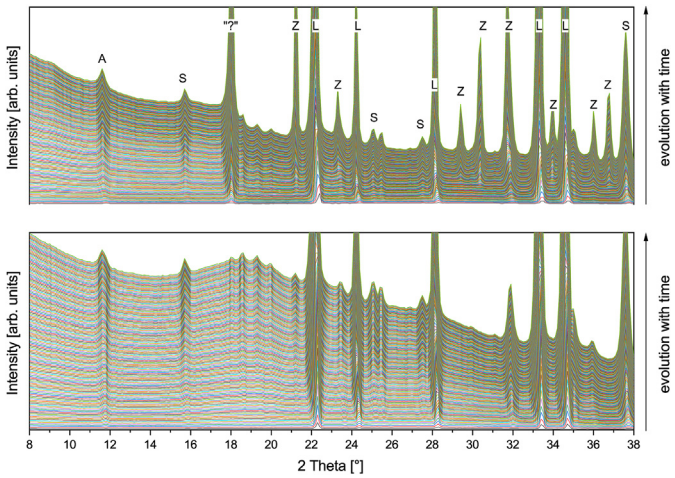

Fig. 7. In-situ XRD investigation of hydrating lithium aluminate paste, either exposed to air (top) or covered with Kapton foil (bottom). In both experiments, γ-$LiAlO_2$ (L) dissolves, while $LiAl_5O_8$ (S) remains stable and $Li_2Al_4(OH)_{12}(CO_3)\cdot 3H_2O$ (A) forms. When exposed to air, zabuyelite (Z) and an unidentified phase (labelled "?") form in addition. The arrows on the right side indicate the direction of evolution of the diffractograms with time.

hydroxides are known to be cementitious phases, i.e. able to impart mechanical strength to a material, it is reasonable to assume that the $Li_2Al_4(OH)_{12}(CO_3)\cdot 3H_2O$ is also responsible for the strength development of the LIS-produced parts. However, the concentration of $Li_2Al_4(OH)_{12}(CO_3)\cdot 3H_2O$ is evidently too low to be detected using conventional XRD measurements, particularly against broad background signals in the XRD patterns from microsilica and possibly L-A-S-H gel, which is the reason that it was not identified as reaction product in the previous study of these materials [25].

Due to the strong increase of the pH of the solution during dissolution of γ-$LiAlO_2$, the microsilica in the slurry is expected to (partially) dissolve during the LIS process as well. As a result of Si, Al and Li in solution, a L-A-S-H gel may form in addition to the $Li_2Al_4(OH)_{12}(CO_3)\cdot 3H_2O$. The Raman spectra of the binder phase are consistent with the presence of such a gel, but are not sufficient to prove its presence unequivocally because of significant overlap of the diagnostic signals of L-A-S-H gel and $Li_2Al_4(OH)_{12}(CO_3)\cdot 3H_2O$.

The present results help to explain the considerable mechanical strength of parts produced by LIS of lithium aluminate/microsilica slurries and may, thus, aid further developments in additive manufacturing of precursors for lithium aluminosilicate glasses and glass ceramics [4] as well as additive manufacturing of alkali-activated materials based on solutions of alkali metals other than Li (namely Na or K).

Declaration of competing interest

The authors declare that they have no known competing financial interests or personal relationships that could have appeared to influence the work reported in this paper.

Acknowledgements

The authors acknowledge technical assistance by Claudia Crasselt and Nico Vogler with the Raman measurements and the TGA measurements, respectively. Philipp Drabetzki and Thi Bao Hoa Dao are thanked for their support during sample preparation and synthesis of the reference materials. This research was supported by Bundesanstalt für Materialforschung und -prüfung (BAM), Germany through the TF program (project 'AFChem').

References

[1] P.K. Subramanian, H.L. Marcus, Selective laser sintering of alumina using aluminum binder, Mater. Manuf. Process. 10 (1995) 689–706, https://doi.org/10.1080/10426919508935060.
[2] P. Stierlen, P. Schanz, P. Eyerer, Si/SiC-ceramic low process shrinkage - high temperature material for the Laser Sinter process. International Solid Freeform Fabrication Symposium, 1998.
[3] A. Gahler, J.G. Heinrich, J. Günster, Direct laser sintering of Al_2O_3-SiO_2 dental ceramic components by layer-wise slurry deposition, J. Am. Ceram. Soc. 89 (2006) 3076–3080, https://doi.org/10.1111/j.1551-2916.2006.01217.x.
[4] A. Zocca, C.M. Gomes, E. Bernardo, R. Müller, J. Günster, P. Colombo, LAS glass-ceramic scaffolds by three-dimensional printing, J. Eur. Ceram. Soc. 33 (2013) 1525–1533, https://doi.org/10.1016/j.jeurceramsoc.2012.12.012.
[5] D. Klosterman, R. Chartoff, N. Osborne, G. Graves, Automated fabrication of monolithic and ceramic matrix composites via laminated object manufacturing (LaM). International Solid Freeform Fabrication Symposium, 1997.
[6] C.M. Gomes, C.R. Rambo, A.P.N. de Oliveira, D. Hotza, D. Gouvea, N. Travitzky, P. Greil, Colloidal processing of glass-ceramics for laminated object manufacturing, J. Am. Ceram. Soc. 92 (2009) 1186–1191, https://doi.org/10.1111/j.1551-2916.2009.03035.x.
[7] M.L. Griffith, T.-M. Chu, W. Wagner, J.W. Halloran, Ceramic stereolithography for investment casting and biomedical applications. International Solid Freeform Fabrication Symposium, 1995.
[8] A.M. Watjen, P. Gingter, M. Kramer, R. Telle, Novel prospects and possibilities in additive manufacturing of ceramics by means of direct inkjet printing, Adv. Mech. Eng. 6 (2014) 141346, https://doi.org/10.1155/2014/141346.
[9] T. Schlordt, S. Schwanke, F. Keppner, T. Fey, N. Travitzky, P. Greil, Robocasting of alumina hollow filament lattice structures, J. Eur. Ceram. Soc. 33 (2013) 3243–3248, https://doi.org/10.1016/j.jeurceramsoc.2013.06.001.
[10] P. Shakor, S. Nejadi, G. Paul, S. Malek, Review of emerging additive manufacturing technologies in 3D printing of cementitious materials in the construction industry, Front. Built Environ. 4 (2019) 85, https://doi.org/10.3389/fbuil.2018.00085.
[11] B. Panda, S.C. Paul, M.J. Tan, Anisotropic mechanical performance of 3D printed fiber reinforced sustainable construction material, Mater. Lett. 209 (2017) 146–149, https://doi.org/10.1016/j.matlet.2017.07.123.
[12] A. Bagheri, C. Cremona, Formulation of mix design for 3D printing of geopolymers: a machine learning approach, Mater. Adv. 1 (2020) 720–727, https://doi.org/10.1039/d0ma00036a.
[13] G. Franchin, P. Scanferla, L. Zeffiro, H. Elsayed, A. Baliello, G. Giacomello, M. Pasetto, P. Colombo, Direct ink writing of geopolymeric inks, J. Eur. Ceram. Soc. 37 (2017) 2481–2489, https://doi.org/10.1016/j.jeurceramsoc.2017.01.030.
[14] Q.L. Sun, Z.Z. Yang, H. Cheng, Y. Peng, Y.Q. Huang, M.X. Chen, Creation of three-dimensional structures by direct ink writing with kaolin suspensions, J. Mater. Chem. C 6 (2018) 11392–11400, https://doi.org/10.1039/c8tc03152e.
[15] B. Panda, S.C. Paul, N.A.N. Mohamed, Y.W.D. Tay, M.J. Tan, Measurement of tensile bond strength of 3D printed geopolymer mortar, Measurement 113 (2018) 108–116, https://doi.org/10.1016/j.measurement.2017.08.051.
[16] G.J.G. Gluth, W.D.A. Rickard, S. Werner, S. Pirskawetz, Acoustic emission and microstructural changes in fly ash geopolymer concretes exposed to simulated fire, Mater. Struct. 49 (2016) 5243–5254, https://doi.org/10.1617/s11527-016-0857-x.
[17] M.B. Watolla, G.J.G. Gluth, P. Sturm, W.D.A. Rickard, S. Krüger, B. Schartel, Intumescent geopolymer-bound coatings for fire protection of steel, J. Ceram. Sci. Technol. 8 (2017) 351–364, https://doi.org/10.4416/Jcst2017-00035.
[18] P. Sturm, G.J.G. Gluth, S. Simon, H.J.H. Brouwers, H.C. Kühne, The effect of heat treatment on the mechanical and structural properties of one-part geopolymer-zeolite composites, Thermochim. Acta 635 (2016) 41–58, https://doi.org/10.1016/j.tca.2016.04.015.
[19] P. Sturm, G.J.G. Gluth, C. Jäger, H.J.H. Brouwers, H.C. Kühne, Sulfuric acid resistance of one-part alkali-activated mortars, Cement Concr. Res. 109 (2018) 54–63, https://doi.org/10.1016/j.cemconres.2018.04.009.
[20] G.J.G. Gluth, P. Sturm, S. Greiser, C. Jäger, H.C. Kühne, One-Part Geopolymers and aluminosilicate gel-zeolite composites based on silica: factors influencing microstructure and engineering properties, in: J. Wang, W. Kriven, T. Fey, P. Colombo, W.J. Weber, J. Amoroso, W.G. Fahrenholtz, K. Shimamura, M. Halbig, S. Kirihara, Y. Wu, K. Shurgart (Eds.), Proceeding of the 42nd International Conference on Advanced Ceramics and Composites, Wiley, Hoboken, 2019, pp. 183–196, https://doi.org/10.1002/9781119543381.ch17.
[21] J.L. Provis, A. Palomo, C.J. Shi, Advances in understanding alkali-activated materials, Cement Concr. Res. 78 (2015) 110–125, https://doi.org/10.1016/j.cemconres.2015.04.013.
[22] S.J. O'Connor, K.J.D. MacKenzie, Synthesis, characterisation and thermal behaviour of lithium aluminosilicate inorganic polymers, J. Mater. Sci. 45 (2010) 3707–3713, https://doi.org/10.1007/s10853-010-4383-x.
[23] A.A. Nourbakhsh, K.J.D. Mackenzie, A. Jamshidi, A novel method for the formation of lithium aluminosilicate and lithium aluminosilicate-alumina matrix composites by silicothermal reaction of Li-geopolymers, Mol. Cryst. Liq. Cryst. 577 (2013) 116–126, https://doi.org/10.1080/15421406.2013.782208.
[24] A. Karrech, M. Dong, M. Elchalakani, M.A. Shahin, Sustainable geopolymer using lithium concentrate residues, Construct. Build. Mater. 228 (2019), https://doi.org/10.1016/j.conbuildmat.2019.116740.
[25] P. Hlaváček, G.J.G. Gluth, J. Lüchtenborg, P. Sturm, T. Mühler, H.C. Kühne, J. Günster, A novel approach to additive manufacturing of alkali-activated materials: laser-induced slip casting (LIS) of lithium aluminate/silica slurries, Ceram. Mod. Technol. 1 (2019) 138–144, https://doi.org/10.29272/cmt.2018.0011.

[26] R. Blachnik, Taschenbuch für Chemiker und Physiker, in: E. Lax (Ed.), Elemente, anorganische Verbindungen und Materialien, Minerale, founded by J. D'Ans vol. 3, Springer, Berlin, 1998.
[27] J. Cheng, L. Guo, S. Xu, R. Zang, Submicron y-$LiAlO_2$ powder synthesized from boehmite, Chin. J. Chem. Eng. 20 (2012) 776–783, https://doi.org/10.1016/S1004-9541(11)60248-6.
[28] B. Walkley, R. San Nicolas, M.A. Sani, J.D. Gehman, J.S.J. van Deventer, J.L. Provis, Synthesis of stoichiometrically controlled reactive aluminosilicate and calcium-aluminosilicate powders, Powder Technol. 297 (2016) 17–33, https://doi.org/10.1016/j.powtec.2016.04.006.
[29] Match! - phase Analysis using powder diffraction, crystal impact - dr. H. Putz & dr. K, Brandenburg GbR Kreuzherrenstr. 102 (2020) 53227. Bonn, Germany, http://www.crystalimpact.com/match.
[30] S. Gates-Rector, T. Blanton, The Powder Diffraction File: a quality materials characterization database, Powder Diffr. 34 (2019) 352–360, https://doi.org/10.1017/s0885715619000812.
[31] V.Y. Karpenko, E.S. Zhitova, L.A. Pautov, A.A. Agakhanov, O.I. Siidra, M.G. Krzhizhanovskaya, V.A. Rassulov, V.N. Bocharov, Akopovaite, $Li_2Al_4(OH)_{12}(CO_3)(H_2O)_3$, a new Li-member of the hydrotalcite supergroup from Turkestan Range, Kyrgyzstan, Mineral. Mag. 84 (2020) 301–311, https://doi.org/10.1180/mgm.2020.10.
[32] C. Calahoo, J.W. Zwanziger, I.S. Butler, Mechanical structural investigation of ion-exchanged lithium silicate glass using micro-Raman spectroscopy, J. Phys. Chem. C 120 (2016) 7213–7232, https://doi.org/10.1021/acs.jpcc.6b01720.
[33] T. Seuthe, M. Grehn, A. Mermillod-Blondin, H.J. Eichler, J. Bonse, M. Eberstein, Structural modifications of binary lithium silicate glasses upon femtosecond laser pulse irradiation probed by micro-Raman spectroscopy, Opt. Mater. Express 3 (2013) 755, https://doi.org/10.1364/ome.3.000755.
[34] C.R. Hubbard, R.L. Snyder, Rir - measurement and use in quantitative XRD, Powder Diffr. 3 (1988) 74–77, https://doi.org/10.1017/S0885715600013257.
[35] C.A. Drewien, D.R. Tallant, O. Eatough, Thermal stability and decomposition kinetics of $Li_2Al_4CO_3(OH)_{12}\cdot 3H_20$, J. Mater. Sci. 31 (1996) 4321–4325, https://doi.org/10.1007/BF00356456.
[36] T. Sato, Thermal decomposition of aluminium hydroxides, J. Therm. Anal. 32 (1987) 61–70, https://doi.org/10.1007/BF01914548.